

GRB 130606A within a sub-DLA at redshift 5.91

A. J. Castro-Tirado^{1,2}, R. Sánchez-Ramírez¹, S. L. Ellison³, M. Jelínek¹, A. Martín-Carrillo⁴, V. Bromm⁵, J. Gorosabel^{1,6,7}, M. Bremer⁸, J. M. Winters⁸, L. Hanlon⁴, S. Meegan⁴, M. Topinka⁴, S. B. Pandey⁹, S. Guziy^{10,1}, S. Jeong¹, E. Sonbas¹¹, A. S. Pozanenko¹², R. Cunniffe¹, R. Fernández-Muñoz¹³, P. Ferrero¹, N. Gehrels¹⁴, R. Hudec^{15,16}, P. Kubánek¹⁷, O. Lara-Gil¹, V. F. Muñoz-Martínez², D. Pérez-Ramírez¹⁸, J. Štrobl^{15,16}, C. Álvarez-Iglesias^{19,20}, R. Inasaridze²¹, V. Rumyantsev²², A. Volnova¹², S. Hellmich²³, S. Mottola²³, J. M. Castro Cerón²⁴, J. Cepa^{19,20}, E. Göğüş²⁵, T. Güver²⁶, Ö. Önal Taş²⁶, I. H. Park²⁷, L. Sabau-Graziati²⁸, and A. Tejero^{19,20}

¹ Instituto de Astrofísica de Andalucía (IAA-CSIC), Glorieta de la Astronomía s/n, E-18008, Granada, Spain
e-mail: ajct@iaa.es

² Unidad Asociada Departamento de Ingeniería de Sistemas y Automática, E.T.S. de Ingenieros Industriales, Universidad de Málaga, Spain.

³ University of Victoria, Department of Physics and Astronomy, P.O. Box 1700 STN CSC, Victoria, BC, V8W 2Y2, Canada.

⁴ UCD School of Physics, University College Dublin, Belfield, Dublin 4, Ireland.

⁵ Department of Astronomy, University of Texas, 2511 Speedway, Austin, TX 78712, USA.

⁶ Unidad Asociada Grupo Ciencias Planetarias UPV/EHU-IAA-CSIC, Departamento de Física Aplicada I, E.T.S., Ingeniería, Universidad del País Vasco UPV/EHU, Bilbao, Spain.

⁷ Ikerbasque, Basque Foundation for Science, Bilbao, Spain.

⁸ Institute de Radioastronomie Millimétrique (IRAM), 300 rue de la Piscine, 38406 Saint Martin d' Hères, France.

⁹ Aryabhata Research Institute of Observational Sciences, Manora Peak, Nainital - 263 002, India.

¹⁰ Nikolaev National University, Nikolska 24, Nikolaev, 54030, Ukraine.

¹¹ Department of Physics, University of Adiyaman, 02040 Adiyaman, Turkey.

¹² Space Research Institute of RAS, Profsoyuznaya, 84/32, Moscow 117997, Russia.

¹³ Instituto de Hortofruticultura Subtropical y Mediterránea "La Mayora", Universidad de Málaga - Consejo Superior de Investigaciones Científicas (IHSM, UMA-CSIC), E-29750 Algarrobo-Costa (Málaga), Spain.

¹⁴ NASA/GSFC, 8800 Greenbelt Road, Code 661, Bldg 34, Rm S254, Greenbelt, Maryland 20771, USA.

¹⁵ Astronomical Institute, Academy of Sciences of the Czech Republic, Ondřejov, Czech Republic.

¹⁶ Czech Technical University in Prague, Faculty of Electrical Engineering, Prague, Czech Republic.

¹⁷ Fyzikální ústav AV ČR, v. v. i. Na Slovance 1999/2, 182 21 Praha 8, Czech Republic.

¹⁸ Facultad de Ciencias Experimentales, Universidad de Jaén, Campus Las Lagunillas, E-23071 Jaén, Spain.

¹⁹ Instituto de Astrofísica de Canarias (IAC), C/. Via Láctea s/n, E-38205 La Laguna (Tenerife), Spain.

²⁰ Departamento de Astrofísica, Universidad de La Laguna, C/. Molinos de Agua s/n, E-38200, Tenerife, Spain.

²¹ Abastumani Astrophysical Observatory of Ilia State University G. Tsereteli Street 3, Tbilisi 0162, Georgia Republic.

²² SRI Crimean Astrophysical Observatory, 98409, Crimea, Nauchny, Ukraine.

²³ Institute of Planetary Research, DLR, Rutherfordstrasse 2, 12489 Berlin, Germany.

²⁴ European Space Astronomy Centre (ESA-ESAC), Camino bajo del Castillo, s/n, Villafranca del Castillo, E-28.692 Villanueva de la Cañada (Madrid), Spain.

²⁵ Sabanc University, Orhanlı - Tuzla, İstanbul 34956, Turkey.

²⁶ İstanbul University, Faculty of Science, Department of Astronomy and Space Sciences, 34119 University, İstanbul, Turkey.

²⁷ Department of Physics, Sungkyunkwan University, Suwon, Korea.

²⁸ Instituto Nacional de Técnica Aeroespacial (INTA), Ctra. de Ajalvir, km. 4, E-28850 Torrejón de Ardoz, Spain.

Received Dec XX, 2013; accepted Month Day, 2014

ABSTRACT

Context. Events such as GRB 130606A at $z = 5.91$, offer an exciting new window into pre-galactic metal enrichment in these very high redshift host galaxies.

Aims. We study the environment and host galaxy of GRB 130606A, a high- z event, in the context of a high redshift population of GRBs.

Methods. We have obtained multiwavelength observations from radio to gamma-ray, concentrating particularly on the X-ray evolution as well as the optical photometric and spectroscopic data analysis.

Results. With an initial Lorentz bulk factor in the range $\Gamma_0 \sim 65$ -220, the X-ray afterglow evolution can be explained by a time-dependent photoionization of the local circumburst medium, within a compact and dense environment. The host galaxy is a sub-DLA ($\log N(\text{H I}) = 19.85 \pm 0.15$), with a metallicity content in the range from $\sim 1/7$ to $\sim 1/60$ of solar. Highly ionized species (N V and Si IV) are also detected.

Conclusions. This is the second highest redshift burst with a measured GRB-DLA metallicity and only the third GRB absorber with sub-DLA HI column density. GRB 'lighthouses' therefore offer enormous potential as backlighting sources to probe the ionization and metal enrichment state of the IGM at very high redshifts for the chemical signature of the first generation of stars.

Key words. gamma-ray burst:general

1. Introduction

It has been recently suggested (Cooke et al. 2011a) that very metal-poor damped Lyman-alpha (DLA) systems (regions of high column density of neutral gas at high redshifts (Wolfe et al. 2005)) could bear the chemical signature of the first generation of stars (Population III stars, Bromm et al. (2009)) born a few hundred million years after the Big Bang. Indeed, it has been suggested that metal-free regions persist to values of $z \leq 6$, allowing Pop III stars with masses in the range 140-260 solar masses to be observed as pair-production instability supernovae (Scannapieco et al. 2005), although a core-collapse (Type II) supernova instead is also plausible (Wang et al. 2012). In spite of the fact that no GRB has so far been firmly associated with a Pop III collapse yet, the high z values found for several GRBs reinforce the potential of GRBs to provide bright background sources to illuminate the early intergalactic medium at a time when quasars were too rare and dim to serve this purpose.

A ~ 275 s cosmic gamma-ray burst (GRB 130606A) was recorded by *Swift* and *KONUS-Wind* on 6 June 2013, 21:04:34 U.T. (T_0) (Barthelmy et al. 2013; Golenetskii et al. 2013), displaying a bright afterglow (the emission at other wavelengths following the gamma-rays) in X-rays, but no apparent optical transient emission (Ukwatta et al. 2013) in the range of the UVOT telescope aboard *Swift*. The TELMA 0.6m diameter telescope at the BOOTES-2 station automatically responded to the alert and an optical counterpart was identified (Jelinek et al. 2013), thanks to the spectral response of the detector up to 1 μm , longer than that of *Swift*/UVOT (0.17-0.65 μm).

The detection of the afterglow at BOOTES-2/TELMA prompted spectroscopic observations with the 10.4m Gran Telescopio Canarias (GTC) starting 1.4 hr after the event, which revealed a very distant explosion at a very high redshift ($z \sim 6$) (Castro-Tirado et al. 2013a), a value later refined to $z = 5.9135 \pm 0.0005$ (Castro-Tirado et al. 2013b), when the Universe was only ~ 950 million years old.

In this work we provide details (Section 2) of the optical imaging and spectroscopic observations beginning a few minutes after the onset of this distant explosion, as well as publicly available γ /X-ray data from the *Swift* satellite, complemented with additional millimetre observations. Results are presented in Section 3 and conclusions in Section 4.

2. Observations

2.1. Optical Observations

2.1.1. Photometry

Early time prompt optical observations were carried out by the Watcher telescope starting on June 6, 21:06:49 U.T., i.e. ~ 135 s after the first *Swift*/BAT trigger ($T_0 = 21:04:34$ UT). The BOOTES-2/TELMA observations, which resulted in the optical afterglow discovery, started on June 6, 21:17:33 U. T., i.e. ~ 660 s after the first *Swift*/BAT trigger. The Watcher observations partially cover the second *Swift*/BAT peak. Additional Johnson R and V-band images were acquired with the 1.23m telescope of Calar Alto (CAHA) observatory, Spain. Late epoch optical observations were obtained with the 0.7m Abastumani Observatory, the AZT-11 (1.25m) telescope at SRI Crimean Astrophysical Observatory, the T100 (1m) telescope at TÜBITAK National Observatory, the 1.5m OSN telescope at Observatorio de Sierra Nevada and with the 10.4m Gran Telescopio Canarias (GTC) equipped with the OSIRIS imaging spectrograph (Fig. 1). Optical photometry is based on isophotal

corrected photometry by IRAF/PHOT31 against standard reference Landolt fields imaged at the 1.5m OSN telescope in order to provide reference stars in the field (Table 1). The photometric results of the afterglow are tabulated in Table 2.

2.1.2. Spectroscopy

Starting 1.3 hr post-burst, optical spectra were obtained on 6 June 2013 with the 10.4m GTC using the R1000B and R500R grisms (1×450 s exposures) and R2500I ($2 \times 1,200$ s exposures) of the OSIRIS imaging spectrograph. The later one provides a nominal resolution of $\sim 120 \text{ km s}^{-1}$. The log is given in Table 3. The 1" wide slit was positioned on the location of the transient source and a 2×2 binning mode was used. The GTC spectra were reduced and calibrated following standard procedures using custom tools based on IRAF and Python. Standard spectrophotometric stars used for flux calibration were Feige 92 for observations for the R1000B grism and Ross 640 for the prisms R500R and R2500I, taken the same night. All spectra were scaled in flux to correct for slit losses using the photometry of the corresponding acquisition images. The final wavelength calibration is on a vacuum scale, appropriate for the application of rest-frame UV atomic data.

2.2. Near-IR observations

Near-IR observations were conducted on July 22 at the 3.5m telescope (+ OMEGA 2000) at the German-Spanish Calar Alto (CAHA) Observatory, with a 5,400s overall exposure time in the H-band. The photometric calibration is based on the observation of the standard S889-E (Persson et al. 1998) and the result is given in Table 2 at an airmass similar to the GRB field.

2.3. Millimetre observations

Target-of-Opportunity millimetre observations were carried out at the Plateau de Bure Interferometer (PdBI) (Guilloteau et al. 1992). It was pointed to the GRB 130606A location on two occasions in its compact 6 antenna configuration. The millimetre counterpart was detected 3.30 days after the GRB onset with a high (~ 10) S/N ratio, on the phase center coordinates (J2000, R.A. = RA: 16:37:35.13; Dec: +29:47:46.5). The results of UV-plane point source fits to the phase center are given in Table 4.

The millimetre afterglow was detected with a flux density of ~ 1.5 mJy at 3 mm, confirming the detection earlier reported at centimetre wavelengths (Laskar et al. 2013). The source became undetectable by June 14.

2.4. X-ray observations

The *Swift* X-ray Telescope (XRT) started collecting data in window timing mode (WT) ~ 60 s after the initial BAT trigger on June 6 at 21:05:35 UT, switching to photon counting mode (PC) after ~ 500 s. The position of the source was monitored up to $\sim 3 \times 10^5$ s post-trigger. The data were processed using the *Swift* software v.2.6. A cleaned event file was generated using the default pipeline, which removes the effects of hot pixels and Earth brightness. From this cleaned event list, the source and background light curves and spectra were extracted from a region of 20 using xselect. In general, no pile-up was found in either the WT or the PC data. The data have been fit using a fixed Galactic

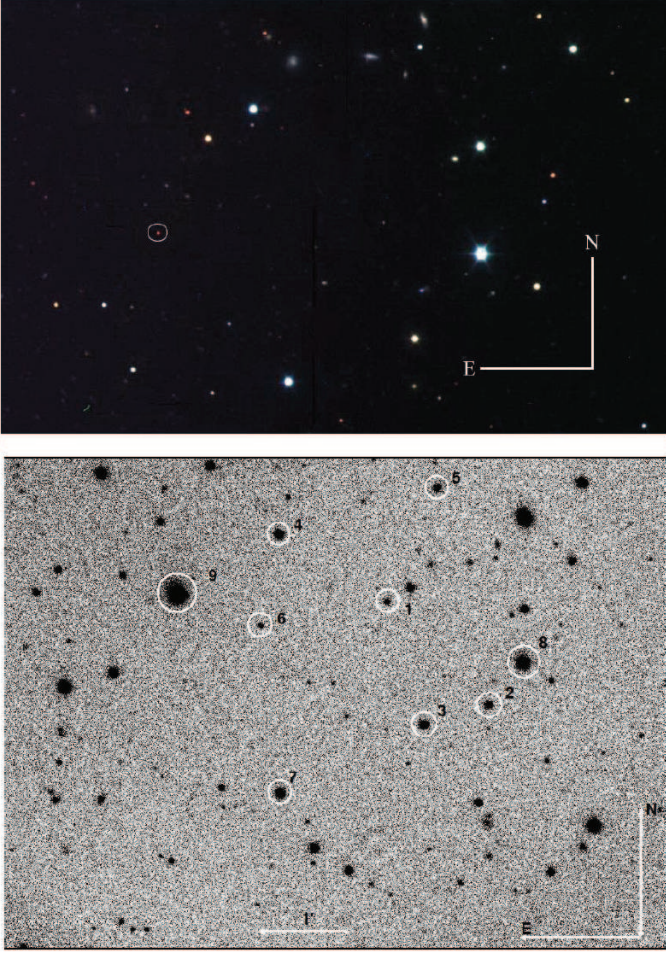


Fig. 1. The colour composite image of the field around GRB 130606A and reference stars in the line of sight. Upper panel: The highly reddened GRB afterglow (circled) and the surrounding field, based on gri images obtained at the 10.4m GTC on June 7, 2013. The field of view is 3.8×2.8 arcmin². Lower panel: Reference stars for photometric calibration in the field around GRB 130606A (Table 1). The field of view (r-band image) is 6.8×5.0 arcmin².

column density at 2×10^{20} cm⁻² and a varying column density in the rest frame in the range $2\text{--}6 \times 10^{22}$ cm⁻².

3. Results

Hereafter we consider $H_0 = 73$ km s⁻¹ Mpc⁻¹, $\Omega_\Lambda = 0.73$, $\Omega_m = 0.27$. At the redshift of $z = 5.9135$ (see below), the light travel time was 12,350 Gyr, the age of the Universe at this redshift was 0.95 Gyr and the luminosity distance is 56,365 Mpc.

3.1. The initial bulk Lorentz factor

The 0.6m BOOTES-2/TELMA and 1.23m CAHA colours show clear signs of a high-redshift dropout ($V\text{-}R > 2.2$ in the CAHA case). From the optical light curve depicted in Fig. 2, the optical flux ($F_{opt} \propto t^\alpha$) exhibits a rising phase toward an optical maximum at ~ 7.5 minutes after the BAT trigger. A rising temporal index $\alpha_1 \sim 1.2$ and decaying temporal index of $\alpha_2 \sim -1.25$ are derived, with a break around $t \sim 450$ s. The interstellar medium (ISM) case predicts the rising index to be

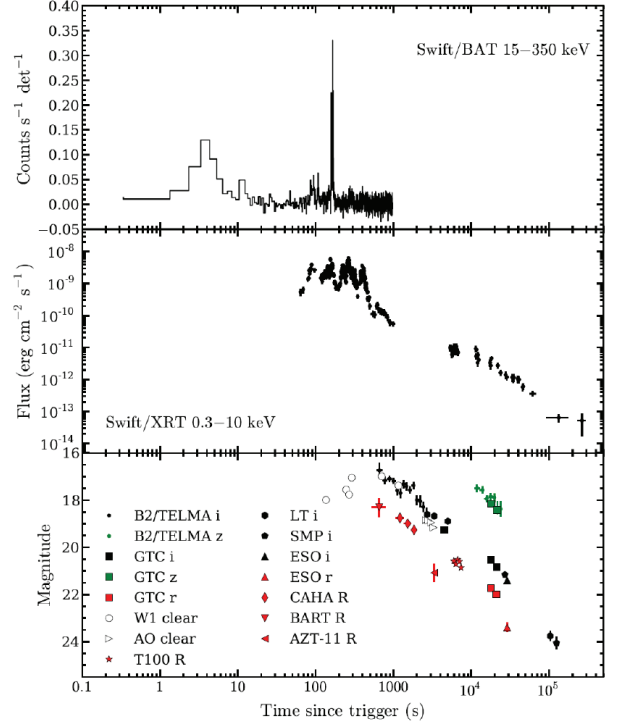


Fig. 2. The GRB 130606A prompt gamma-ray emission and the multiwavelength afterglow evolution. The *Swift*/BAT light curve shows a double-peaked structure with the initial peak lasting ~ 10 s and a brighter second peak at $T_0 + 150$ s of ~ 20 s duration. The gamma-ray lightcurve is compared with the multiwavelength (X-ray, optical) GRB 130606A afterglow lightcurves. Significant temporal (and spectral) evolution is noticeable in the XRT data. The lower panel shows the rising optical afterglow lightcurve based on Watcher data, prior to the well sampled decay, based on the data gathered by BART, BOOTES-2/TELMA, 0.7m AO, T100, 1.23m CAHA, AZT-11, 1.5m OSN and 10.4m GTC (Table 1), complemented with other data published elsewhere (Afonso et al. 2013; Butler et al. 2013; Virgili et al. 2013). The observations were carried out in different optical wavebands (R, r, i, z) or clear (meaning unfiltered) and the initial bulk Lorentz factor to be determined. 1σ error bars are plotted.

~ 2 whereas a wind profile (WIND) case predicts it to be ~ 0.5 (Panaitescu and Vestrand 2011). These values have not been seen in many of the observed cases at early times, possibly due to the early emission being a combination of multiple components such as early time energy injection. Using Eq. 4 of Rykoff et al. (2009) and for $s \sim 4$, the peak time t_{peak} is ~ 350 s. Assuming that the early optical emission is the onset of the forward shock emission, the value of t_{peak} in the rest frame can be used (i.e. $t_{peak}/(1+z)$) to calculate the initial bulk Lorentz factors for the ISM and WIND cases for the GRB environment, following Melandri et al. (2010). We also consider the isotropic energy released in GRB 130606A (at $z \sim 5.91$) to be 28.3 ± 0.5 in units of 10^{52} ergs (Golenetskii et al. 2013). Thus, for $E_{52} \sim 28.3$ and $t_{peak} \sim 350$ s, the bulk Lorentz factor in the ISM case is $\Gamma_0 \sim 185$, whereas in the case of WIND, $\Gamma_0 \sim 65$. Γ_0 can be also estimated from Ghirlanda et al. (2012), giving $\Gamma_0 \sim 160$ for the ISM case and $\Gamma_0 \sim 70$ for the WIND case. Using the statistical relations from Liang et al. (2010) and Lü et al. (2012), we find $\Gamma_0 \sim 185$

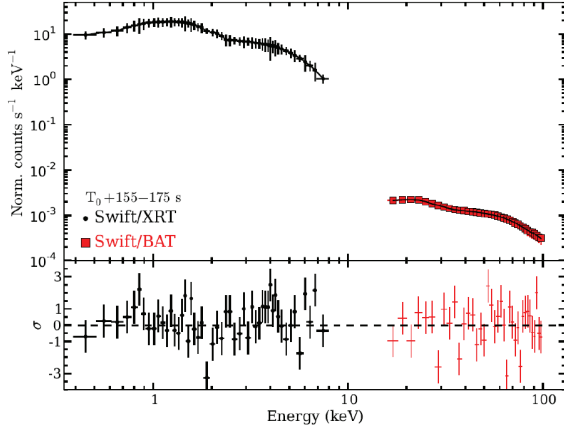


Fig. 3. The GRB 130606A *Swift*/BAT and *Swift*/XRT spectrum. A simple power-law function (black line) yields a formally acceptable fit ($\chi^2/\text{d.o.f.} = 1.29$). The inclusion of a thermal component provides negligible improvement ($\chi^2/\text{d.o.f.} = 1.26$). 1σ error bars are shown.

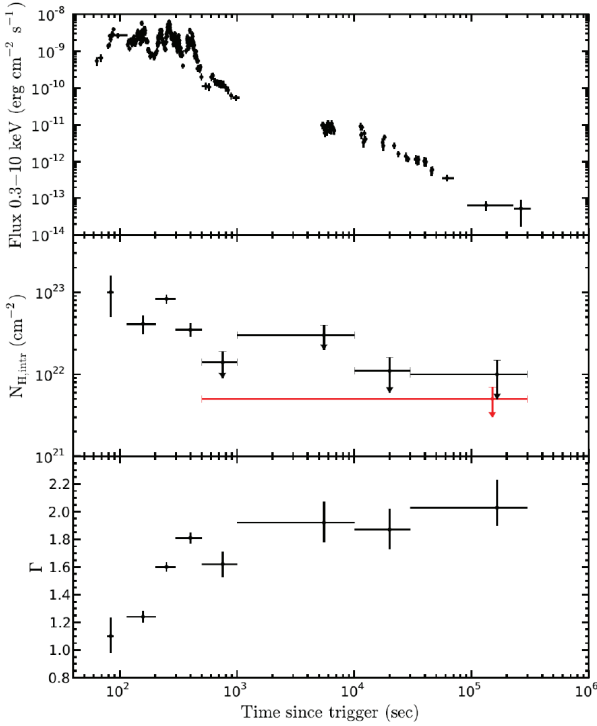


Fig. 4. X-ray light curve for the GRB 130606A afterglow and variations in the power-law index and column density as a function of time. Upper panel: The X-ray afterglow light curve. Middle panel: The decrease of the column density as the gamma/X-ray emission decreases. Lower panel: The variation of the power-law index Γ with respect to the X-ray luminosity showing that the spectrum gets progressively harder as the flux increases. 1σ error bars are shown.

and ~ 220 respectively for the ISM and WIND cases. The post-peak data of the optical light curve exhibits a temporal decay index $\alpha_{opt} \sim 1.3$ along with a superimposed variability.

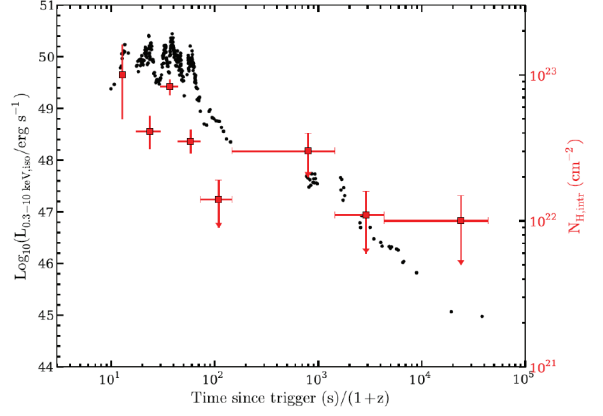


Fig. 5. The GRB 130606A X-ray afterglow and variations in the power-law index and column density. The variation of the N_H column density (squares with red bars) with respect to the X-ray luminosity (black dots). 1σ error bars are shown.

3.2. Temporal and spectral evolution during the *Swift* observation

Swift/XRT observations showed a high hydrogen column density decreasing with time, which can be interpreted as a time-dependent photoionization of the local circumburst medium, within a compact and dense environment, as found in only a few cases.

The XRT light curve (Fig. 2) reveals noticeable variations in the observed count rate that can be divided into 4 segments. The results from the time resolved spectral analysis from the X-ray emission of GRB 130606A are given in Table 5. The dependence of the flux on frequency, ν , and time t , is described through this section and in Table 5 by $F_\nu \propto \nu^{-\beta} t^{-\alpha}$ where $\beta = \Gamma - 1$. Thus, we find the following distinct episodes:

I) Beginning of XRT observations up to $\sim T_0 + 759$ s. This segment is dominated by flaring activity from internal shocks as part of the prompt emission. The combined *Swift*/BAT-XRT X-ray spectrum in the interval $T_0 + 155$ s to $T_0 + 175$ s can be fit using a simple absorbed power law model ($\chi^2/\text{d.o.f.} = 1.29$), and the addition of a thermal component has negligible effect ($\chi^2/\text{d.o.f.} = 1.26$). The best fit model (Fig. 3) has a hydrogen column density $(4 \pm 2) \times 10^{22} \text{ cm}^{-2}$ and a photon index $\Gamma = 1.03 \pm 0.02$.

II) $T_0 + 759$ s to $T_0 + 1300$ s. This is characterised by a fast decay with temporal index, $\alpha_X = 3 \pm 1$, consistent with high-latitude emission (Genet and Granot 2009) at the end of the prompt emission ($\alpha_X = 2 + \beta_X$), where $\alpha_X = 0.62 \pm 0.09$.

III) $T_0 + 1300$ s to $T_0 + 1.6 \times 10^4$ s. During this segment, the X-ray count-rate decay is consistent with a temporal decay index of $\alpha_X = 0.66 \pm 0.20$. This plateau phase is typically associated with late activity from the central engine (Zhang 2007). The end of this plateau phase at $T_0 + 1.6 \times 10^4$ s seems to be achromatic when comparing the X-ray and i-band light curves (Fig. 2) as expected at the end of late activity from the central engine. The closure relations modified with an energy injection parameter, q (Zhang et al. 2006), are consistent with an homogeneous environment (ISM) with $q = 0.5 \pm 0.4$ when $\nu_x < \nu_c$. This value is consistent with previous measurements of q (Zhang et al. 2006; Curran et al. 2009). The electron spectral index inferred during this segment is $p = 2.84 \pm 0.30$, consistent within 1σ with the distribution of values of p presented by Curran et al. (2010) and Starling et al. (2008). The wind model when $\nu_x < \nu_c$ with

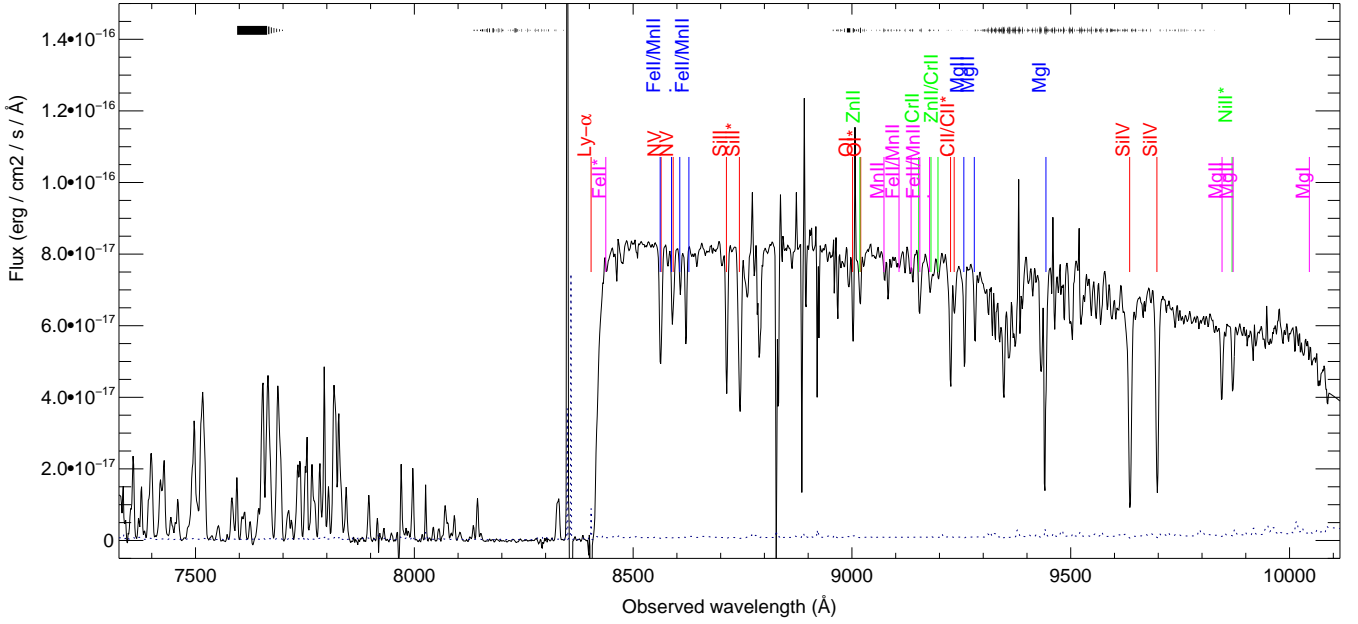


Fig. 6. The 10.4m GTC spectrum ~ 6 hr post-burst. This is the highest resolution spectrum taken for GRB 130606A by GTC, with the R2500I grism (see Table 3 for details). The noise spectrum (dotted line) is also plotted. Intervening systems at redshifts $z = 2.310$ (blue), 2.521 (magenta), 3.451 (green) besides that (a sub-DLA) of the GRB 130606A host galaxy at $z = 5.913$ (red) are plotted. Strong absorption by intergalactic hydrogen in the line of sight is causing the apparent low optical flux observed in the Lyman- α forest region (below 8,400 Å).

late energy injection is rejected for GRB 130606A since the q -parameter inferred is $q < 0$ which does not have physical meaning. The cases when $v_x > v_c$ in the ISM or wind model are also rejected since result in $p < 2$ for which the closure relations are no longer valid. Finally, the optical temporal decay index $\alpha_{opt} \sim 1.3$ is consistent with α_X during this time interval.

IV) $T_0 + 1.6 \times 10^4$ s to $T_0 + 3 \times 10^5$ s. In this segment, the decay ($\alpha_X = 1.86 \pm 0.20$) is consistent with forward shock emission when $v_x < v_c$. The closure relation between the temporal and spectral index in the case of an ISM model for $v_x < v_c$ is $\alpha = 3\beta/2 = 1.55 \pm 0.30$ consistent with the observed α_X . For a wind environment, the relationship can be re-written as $\alpha = (3\beta + 1)/2 = 2.03 \pm 0.30$ which is also consistent with the observed temporal decay. However, the wind environment was tentatively rejected in the previous segment and may not be necessary to explain the afterglow emission of GRB 130606A. The electron spectral index obtained in this segment is, $p = 3.0 \pm 0.4$. This value is consistent with the electron spectral index inferred in the previous segment. It should be noted that during this segment there seems to be small variability in the X-ray light curve in the form of a micro-flare peaking at $\sim T_0 + 4 \times 10^4$ s. As shown in Fig. 4 GRB 130606A shows significant variation in the photon index, Γ and N_H column density throughout the X-ray observations. The variation of Γ with respect to the X-ray luminosity shows that the spectrum gets progressively softer as the flux decreases.

The intrinsic column density N_H is well constrained while the central engine remains active (first 500 s since trigger) implying high levels of photoionization of the local high-density medium. During this time, the observed intrinsic N_H is almost 3 orders of magnitude higher than the galactic column density at these coordinates. Once the prompt emission ends, the intrinsic N_H decreases abruptly and no excess with respect to the galactic

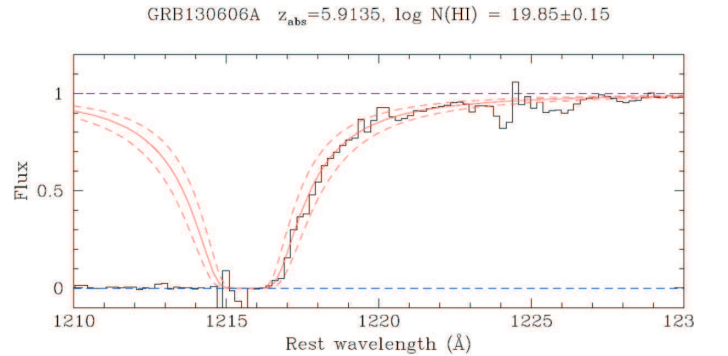


Fig. 7. The N(H I) fit to the GTC (+ OSIRIS) spectrum of GRB 130606A. Taken on June 7, 2013, the figure shows the data (black solid line) and the best fit damped profile (solid red line). The derived column density is $\log N(\text{H I}) = 19.85$, together with the fits for $\log N(\text{H I}) = 19.70$ and 20.00 (dashed red lines).

value can be found for the remainder of the X-ray observations. This can be interpreted as a time-dependent photoionization of the local circumburst medium, within a compact and dense environment, only found in a few GRBs such as GRB 980329 (Lazzati 2002) and GRB 000528 (Frontera et al. 2004).

3.3. The GRB 130606A sub-DLA host galaxy

In order to determine the neutral hydrogen content at the GRB host galaxy redshift, the Lyman-alpha line observed in the GTC optical spectrum (Fig. 6) was fitted with a damped profile and a value of $\log N(\text{H I}) = 19.85 \pm 0.15$ was derived (Fig. 7), in

good agreement with two independent data-sets (Chornock et al. 2013; Totani et al. 2013). The associated system is therefore technically classified as a sub-DLA.

Besides structure in the Lyman forest region (discussed in Chornock et al. (2013)), the GTC optical spectrum shows a variety of absorption lines at different redshifts (e.g. 2.310, 2.521, 3.451), but we will concentrate on the GRB 130606A system at $z = 5.9135$ that is associated with the host galaxy.

The high signal-to-noise ratio (SNR) of the GTC spectrum permitted a search for relatively weak metal lines, and offers an improvement over some of the limits measured by Chornock et al. (2013).

In the case of sulphur, the triplet at 1250, 1253, 1259 Å can be used. Significant absorption is detected at the position of the weakest of these three lines (1250 Å), but the lack of absorption at 1253 Å indicates that the absorption is likely from a contaminating source. Based on the non-detection of the S II 1253 Å line, we determine an observed frame 3σ EW limit < 0.157 Å (assuming a FWHM = 3.4 Å and a S/N of 65 in the S II line region) which corresponds to 0.023 Å in the rest frame. The rest-frame EW limit yields $\log N(\text{S II}) < 14.17$. Assuming $N(\text{H I}) = 19.85$ and solar $S/\text{H} = 4.85$ (from Asplund et al. (2009)) this gives a 3σ upper limit $[S/\text{H}] < -0.82$, which is 0.3 dex (a factor of ~ 2) deeper than the sulphur limit obtained by Chornock et al. (2013).

In addition to the upper limit to the sulphur abundance, we can determine lower limits to the abundances of oxygen and silicon. The limiting silicon abundance is determined from the mildly saturated Si II 1260 Å line with a rest frame EW=0.35 Å, yielding $[\text{Si}/\text{H}] > -1.80$, without consideration of ionization or dust depletion corrections. The oxygen abundance is determined from the O I 1302 Å line, which is also likely to be partly saturated despite its modest EW (0.2 Å). The fact that O I doesn't require an ionization correction and O does not deplete, means that this is one of the best lines from which to obtain an accurate metallicity. The major uncertainty here is that it is close to a small noise feature on the red side which might lead to an overestimate of the oxygen abundance at the 0.1 dex level. Taking these factors into account, we determine $[\text{O}/\text{H}] > -2.06$. The Si and O limits are consistent to within 0.1 dex of the values independently derived (from different spectra) by Chornock et al. (2013). Combined with the upper limit from sulphur, we can constrain the metallicity within a factor of about 10, in the range from $\sim 1/7$ to $\sim 1/60$ of solar.

For a more comprehensive study of the abundances, we refer to Hartog et al. (2013). Furthermore, we also point out that it is very likely that the gas is partially ionized: strong high-ionization lines (such as Si IV and N V) are present at the redshift of the absorber.

4. Conclusions

With an initial Lorentz bulk factor in the range $\Gamma_0 \sim 65$ -220, the X-ray afterglow evolution can be explained by a time-dependent photoionization of the local circumburst medium, within a compact and dense environment. The host galaxy is a sub-DLA ($\log N(\text{H I}) = 19.85 \pm 0.15$), and a metallicity content in the range from $\sim 1/7$ to $\sim 1/60$ of solar is inferred.

In order to place the chemistry of the GRB sub-DLA in context with other high z absorbers, both Fig. 8 and Fig. 9 show the metallicity of a compilation of GRB host galaxy absorption systems (GRB-DLAs) compared to quasars with DLA and sub-DLAs (QSO-DLAs), combining the data reported in the litera-

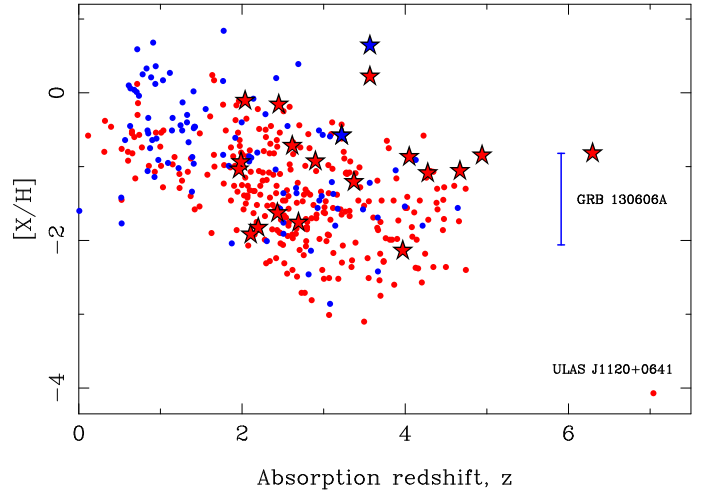


Fig. 8. The metallicity ($[X/H]$) as a function of redshift is shown for a compilation of QSO-DLAs (circles) and GRB-DLAs (stars, Schady et al. (2011); Thöne et al. (2013)), including the location for GRB 130606A at $z = 5.9$ (blue error bar) and ULAS J1120+0641 at $z \sim 7$ (Simcoe et al. 2012). The GRB 130606A sub-DLA is the 2nd highest redshift burst with a measured GRB-DLA metallicity and only the third GRB absorber with sub-DLA HI column density. Blue colours are used for $\log N(\text{HI}) < 20.3$ and red is used for $\log N(\text{H I}) \geq 20.3$. In order of preference for any given absorber, Zn, S, O, Si, Fe+0.4 dex is our choice of metallicity indicator, where the 0.4 offset for Fe accounts for typical dust depletion.

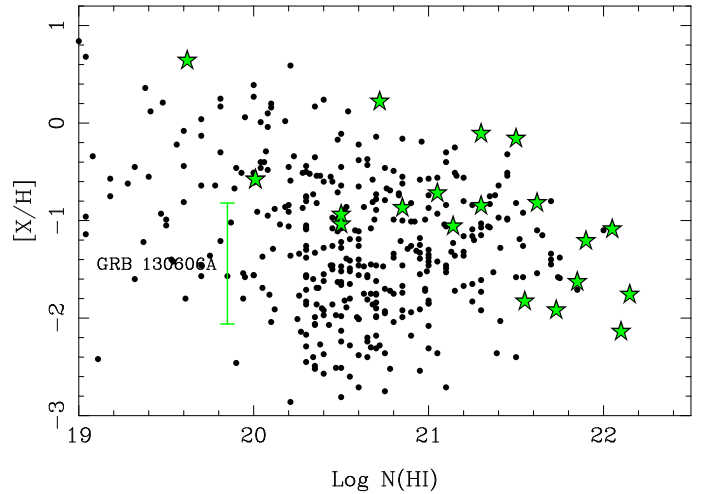


Fig. 9. The metallicity of a GRB sample (green stars) versus $N(\text{H I})$ compared to a sample of DLAs (black dots). Adapted from Schady et al. (2011) and Thöne et al. (2013). The location for GRB 130606A (green error bar) is also plotted.

ture (Schady et al. 2011; Thöne et al. 2013). The GRB 130606A sub-DLA is a rare find: the second highest redshift burst with a measured GRB-DLA metallicity and only the third GRB absorber with sub-DLA HI column density. At $z > 5$, the only other object known with lower metallicity is the ULAS J1120+0641 DLA at $z \sim 7$ (Simcoe et al. 2012). However, the DLA towards ULAS J1120+0641 is close to the redshift of the quasar and its metallicity is determined from a stacked spectrum, both of which complicate its interpretation (Ellison et al. 2010, 2011).

We note that GRB 130606A, given the non-zero metal content of the host, might have originated from a non-Pop III progenitor star, but whether its afterglow light penetrated material that was pre-enriched by Pop III nucleosynthesis at even higher redshifts (Wang et al. 2012) remains uncertain. Indeed several possibilities for the death of the first stars have recently been suggested by theoretical models (Bromm 2013).

Events such as GRB 130606A at $z = 5.91$, and future ones at $z > 10$, offer an exciting new window into pre-galactic metal enrichment in these very high redshift galaxies. These bright lighthouses constitute a significant step forward towards using these sources as beacons for measuring abundances at such early times.

New GRB missions, equipped with on-board near-IR detectors, and coupled to state-of-the-art instruments built for the largest diameter ground-based telescopes, such as the forthcoming CIRCE instrument (Eikenberry et al. 2013) on the 10.4m GTC, will allow us to study the first stars that fundamentally transformed the Universe only a few hundred million years after the Big Bang.

Acknowledgements. Partly based on observations carried out with the 0.6 m TELMA telescope at the BOOTES-2 station in EELM-CSIC, with the 10.4 m Gran Telescopio Canarias instaled in the Spanish Observatorio del Roque de los Muchachos of the Instituto de Astrofísica de Canarias in the island of La Palma (GTC69-13A) and with the IRAM Plateau de Bure Interferometer. IRAM is supported by INSU/CNRS (France), MPG (Germany) and IGN (Spain). We acknowledge the support of F. J. Aceituno (OSN observatory) and of the Spains Ministerio de Ciencia y Tecnología through Projects AYA2009-14000-C03-01/ESP, AYA2011-29517-C03-01 and AYA2012-39727-C03-01 and Creative Research Initiatives of MEST/NRF in Korea (RCMST). R.H. acknowledges GA CR grant 102/09/0997. E.S. acknowledge support by the Scientific and Technological Research Council of Turkey (TÜBİTAK) through the project 112T224. A.P. and A.V. are partially supported by RFBR 12-02-01336, 13-01-92204. LH, AMC and MT acknowledge support from SFI under grants 07/RFP/PHYF295 and 09/RFP/AST/2400 and from the EU FP7 under grant agreement 283783. T.G. acknowledges support from Bilim Akademisi - The Science Academy, Turkey, under the BAGEP program. This study has been developed in the framework of the Unidad Asociada IAA/CSIC-UPV/EHU, supported by the Ikerbasque science foundation. J.G. is partially supported by AYA2012-39362-C02-02. We acknowledge the use of public data from the *Swift* data archives and the service provide by the gamma-ray burst Coordinates Network (GRB) and BACODINE system, maintained by S. Barthelmy.

References

Afonso, P., Kann, D. A., Nicuesa, A. et al. 2013, GRB Coordinates Network, 14807, 1
 Asplund, M., Grevesse, N., Sauval, J. A., & Scott, P. 2009, ARAA, 47, 481
 Barthelmy, S. D., Baumgartner, W. H., Cummings, J. R., et al. 2013, GRB Coordinates Network, 14819, 1
 Berg, T. A. et al. 2013, in preparation
 Bromm, V. 2013, RPPH, 76, 2901
 Bromm, V. & Loeb, A. 2002, ApJ, 575, 111
 Bromm, V. & Loeb, A. 2006, ApJ, 642, 382
 Bromm, V., Yoshida, N., Hernquist, L., & McKee, C. F. 2009, Nature, 459, 49
 Butler, N., Watson, A. M., Kutuyev, A. et al. 2013, GRB Coordinates Network, 14824, 1
 Castro-Tirado, A. J., Sanchez-Ramirez, R., Jelinek, M., et al. 2013a, GRB Coordinates Network, 14790, 1
 Castro-Tirado, A. J., Sanchez-Ramirez, R., Gorosabel, J., et al. 2013b, GRB Coordinates Network, 14796, 1
 Chornock, R., Berger, E., Fox, D. B., et al. 2013, ApJ, 774, 26
 Ciardi, B. & Loeb, A. 2000, ApJ, 540, 687
 Cooke, R., Pettini, M., Steidel, C. C., Rudie, G. C., & Jorgenson, R. A. 2011a, Monthly Notices of the Royal Astronomical Society, 412, 1047
 Cooke, R., Pettini, M., Steidel, C. C., Rudie, G. C., & Nissen, P. E. 2011b, MNRAS, 417, 1534
 Curran, P. A., Evans, P. A., de Pasquale, M., Page, M. J., & van der Horst, A. J. 2010, ApJ, 716, L135
 Curran, P. A., Starling, R. L. C., van der Horst, A. J., & Wijers, R. A. M. J. 2009, Mon. Not. R. Astron. Soc, 395, 580
 Eikenberry, S. S., Lasso, N., Raines, S. N., et al. 2013, RMxAC, 42, 119

Ellison, S., Prochaska, J. X., & Mendel, J. T. 2011, MNRAS, 412, 448
 Ellison, S. L., Prochaska, J. X., Hennawi, J., et al. 2010, MNRAS, 406, 1435
 Fabbian, D., Nissen, P. E., Asplund, M., Pettini, M., & Akerman, C. 2009, A&A, 500, 1143
 Frontera, F., Amati, L., Lazzati, D., et al. 2004, ApJ, 614, 301
 Genet, F. and Granot, J. 2009, MNRAS, 399, 1328
 Ghirlanda, G., Nava, L., Ghisellini, G., et al. 2012, MNRAS, 420, 483
 Golenetskii, S., Aptekar, R., Mazets, E., et al. 2013, GRB Coordinates Network, 14808, 1
 Guilloteau, S., Delannoy, J., Downes, D. et al. 1992, A&A, 262, 624
 Hartog, O. et al. 2013, in preparation
 Jelinek, M., Gorosabel, J., Castro-Tirado, A. J., et al. 2013, GRB Coordinates Network, 14782, 1
 Karlsson, T., Bromm, V., & Bland-Hawthorn, J. 2013, RvMP, 85, 809
 Lamb, D. Q. & Reichart, D. E. 2000, ApJ, 536, L1
 Laskar, T., Zauderer, A., & Berger, E. 2013, GRB Coordinates Network, 14817, 1
 Lazzati, D. & Perna, R. 2002, MNRAS, 330, 383
 Liang, E.-W., Yi, S.-X., Zhang, J., et al. 2010, ApJ, 725, 2209
 Lü, J., Zou, Y.-C., Lei, W.-H., et al. 2012, ApJ, 751, 49
 Mackey, J., Bromm, V., & Hernquist, L. 2003, ApJ, 586, 1
 Melandri, A., Kobayashi, S., Mundell, C. G., et al. 2010, ApJ, 723, 1331
 Panaitescu A. & Vestrand, W. T. 2011, MNRAS, 414, 3537
 Persson S. E., Murphy, D. C., Krzeminski, W., et al. 1998, AJ, 116, 2475
 Rykoff, E. S., Aharonian, F., Akerlof, C. W., et al. 2009, ApJ, 702, 489
 Scannapieco, E., Madau, P., Woosley, S., Heger, A., & Ferrara, A. 2005, ApJ, 633, 1031
 Schady, P., Savaglio, S., Krühler, T., Greiner, J., & Rau, A. 2011, A&A, 525, A113
 Simcoe, R. A., Sullivan, P. W., Cooksey, K. L., et al. 2012, Nature, 492, 79
 Starling, R. L. C., van der Horst, A. J., Rol, E., et al. 2008, ApJ, 672, 433
 Thöne, C. C., Fynbo, J. P. U., Goldoni, P., et al. 2013, MNRAS, 428, 3590
 Totani, T., Aoki, K., Hattori, T. et al. 2013, PASJ, submitted (arXiv:1312.3934v1)
 Ukwatta, T. N., Barthelmy, S. D., Gehrels, N., et al. 2013, GRB Coordinates Network, 14781, 1
 Virgili, F. J., Mundell, C., Melandri, A. & Gomboc, A. 2013, GRB Coordinates Network, 14785, 1
 Wang, F. Y., Bromm, V., Greif, T. H., et al. 2012, ApJ, 760, 27
 Wolfe, A. M., Gawiser, E., & Prochaska, J. X. 2005, ARAA, 43, 861
 Zhang, B. 2007, CJAA, 7, 1
 Zhang, B., Fan, Y. Z., Dyks, J., et al. 2006, ApJ, 642, 354

Table 1. Reference stars in the field of GRB 130606A.

N	R.A.(J2000)	Dec(J2000)	R-band mag	I-band mag	H-band mag
1	16 37 33.7	+29 48 19.0	18.04 ± 0.11	16.36 ± 0.02	14.54 ± 0.05
2	16 37 28.4	+29 47 05.6	16.97 ± 0.07	15.71 ± 0.02	13.95 ± 0.04
3	16 37 31.9	+29 46 53.6	16.41 ± 0.05	16.12 ± 0.02	15.31 ± 0.05
4	16 37 39.4	+29 49 05.6	16.22 ± 0.05	15.88 ± 0.02	15.07 ± 0.05
5	16 37 31.0	+29 49 36.4	17.65 ± 0.09	17.03 ± 0.03	--
6	16 37 40.4	+29 48 03.4	18.62 ± 0.14	18.21 ± 0.04	17.38 ± 0.06
7	16 37 39.5	+29 46 07.7	15.99 ± 0.04	15.66 ± 0.02	--
8	16 37 26.6	+29 47 34.5	14.57 ± 0.02	14.24 ± 0.02	13.54 ± 0.04
9	16 37 44.8	+29 48 25.3	13.11 ± 0.02	12.82 ± 0.02	--

Table 2. Optical and near-IR observations gathered at several astronomical observatories worldwide. RVIH-band magnitudes are given in the Vega system whereas clear and Sloan-filter magnitudes are given in the AB system. Not corrected for Galactic extinction.

Start Time (JD) ^a	Magnitude	Filter	Telescope ^b
2456450.379734	17.99 ± 0.11	clear	0.4m Watcher
2456450.381019	17.55 ± 0.08	clear	
2456450.381273	17.76 ± 0.10	clear	
2456450.381528	17.04 ± 0.06	clear	
2456450.386308	16.99 ± 0.10	clear	
2456450.391528	17.38 ± 0.14	clear	
2456450.382210	> 16.5	R	0.25m BART
2456450.38575	18.30 ± 0.40	R	
2456450.385800	16.73 ± 0.34	i	0.6m TELMA
2456450.387112	17.16 ± 0.16	i	
2456450.388424	17.10 ± 0.13	i	
2456450.389742	17.18 ± 0.12	i	
2456450.391053	17.59 ± 0.20	i	
2456450.392371	17.70 ± 0.20	i	
2456450.393677	17.32 ± 0.16	i	
2456450.395124	17.42 ± 0.16	i	
2456450.396963	17.56 ± 0.15	i	
2456450.399062	17.38 ± 0.15	i	
2456450.401339	17.99 ± 0.21	i	
2456450.403521	18.04 ± 0.24	i	
2456450.406057	18.29 ± 0.21	i	
2456450.408959	18.61 ± 0.30	i	
2456450.514739	17.49 ± 0.15	Z	0.6m TELMA
2456450.537466	17.56 ± 0.16	Z	
2456450.560270	17.93 ± 0.15	Z	
2456450.583792	17.84 ± 0.16	Z	
2456450.606892	17.89 ± 0.17	Z	
2456450.629280	18.32 ± 0.26	Z	
2456450.651610	18.37 ± 0.31	Z	
2456450.392159	18.75 ± 0.03	R	1.23m CAHA
2456450.395772	18.99 ± 0.04	R	
2456450.399383	19.26 ± 0.06	R	
2456450.403071	>21.5	V	1.23m CAHA
2456450.408137	18.84 ± 0.05	clear	0.7m AO
2456450.410694	18.86 ± 0.04	clear	
2456450.413241	18.95 ± 0.05	clear	
2456450.415799	19.16 ± 0.06	clear	
2456450.416655	21.08 ± 0.38	R	1.25m AZT-11
2456450.447046	20.58 ± 0.07	R	1.0m T100
2456450.451171	20.71 ± 0.07	R	
2456450.455296	20.51 ± 0.07	R	
2456450.459379	20.60 ± 0.08	R	
2456450.463463	20.86 ± 0.09	R	
2456450.582700	>25	g	10.4m GTC
2456450.583935	21.73 ± 0.07	r	10.4m GTC
2456450.120092	22.00 ± 0.07	r	
2456450.429560	19.27 ± 0.05	i	10.4m GTC
2456450.584792	20.53 ± 0.05	i	
2456450.621551	20.83 ± 0.05	i	
2456450.585938	18.14 ± 0.08	z	10.4m GTC
2456450.622558	18.42 ± 0.08	z	
2456451.480060	>22.1	I	1.5m OSN
2456496.462500	>21.5	H	3.5m CAHA

Notes. ^(a) Values measured since 21:04:34 UT June 6, epoch of the first *Swift*/BAT trigger time (Julian Date (JD) is 2556450.378171)

^(b) 0.4m Watcher is the 0.4m telescope in Boyden Observatory (South Africa). 0.25m BART is the 0.25m telescope in Astronomical Institute at Ondřejov (Czech Republic). 0.6m TELMA is the 0.6m TELEscopio Malaga in Algarrobo Costa (Málaga, Spain). 0.7m AO is the 0.7m AS-32 telescope in Abastumani Observatory (Georgia). T100 is the 1.0m telescope in TÜBITAK National Observatory (Turkey). AZT-11 is the 1.25m telescope at the SRI Crimean Astrophysical Observatory (Ukraine). 1.5m OSN is the 1.5m telescope at Observatorio de Sierra Nevada in Granada (Spain); 3.5m CAHA is the 3.5m telescope at the German-Spanish Calar Alto Observatory in Almería (Spain); GTC is the 10.4-m Gran Telescopio Canarias in Canary Islands (Spain).

Table 3. Log of Spectroscopic data obtained at the 10.4m GTC.

Start Time (UT)	Exp Time (s)	Grism	Wavelength Range (Å)	Slit width (")	Airmass
06-Jun 2013-22:23:50.5	1 x 450	R1000B	3,650 - 7,750	1.2	1.17
06-Jun 2013-22:32:18.1	1 x 450	R500R	4,750 - 10,300	1.2	1.15
07-Jun 2013-02:10:09.7	2 x 1,200	R2500I	7,320 - 10,100	1.0	1.05

Table 4. Flux densities measured at Plateau de Bure Interferometer.

Time (days post-burst)	Flux density at 3 mm [mJy]	Frequency [GHz]
3.30	1.45 ± 0.15	86.7
7.50	0.03 ± 0.13	86.7

Table 5. Spectral fitting analysis for the *Swift*/XRT X-ray data assuming $N_H(\text{Gal}) = 2 \times 10^{20} \text{ cm}^{-2}$.

Time Interval (after T_0 [s])	$N_H(\text{intrinsic}) [10^{22} \text{ cm}^{-2}]$	Γ	$F_X(\text{unabsorbed})$	χ^2/dof
78-89	10(-5.,+6)	1.10(-0.12,+0.13)	3.25e-09(-0.24,+0.22)	42/43
115-200	4.1(-1.0,+1.1)	1.24(-0.04,+0.04)	2.10e-09(-0.06,+0.06)	241/225
200-300	8.3(-1.0,+1.0)	1.60(-0.03,+0.03)	2.61e-09(-0.05,+0.05)	324/296
300-500	3.5(-0.6,+0.7)	1.81(-0.04,+0.04)	8.88e-10(-0.22,+0.25)	285/244
78-200	5.1(-1.0,+1.1)	1.22(-0.04,+0.04)	2.85e-09(-0.08,+0.09)	261/259
500-1000	< 1.4	1.62(-0.09,+0.09)	1.07e-10(-0.12,+0.05)	24/28
1000-1e4	< 3	1.92(-0.14,+0.15)	8.4e-12(-0.7,+0.7)	26/26
1e4-3e4	< 1.1	1.87(-0.14,+0.15)	2.7e-12(-0.3,+0.3)	27/27
3e4-3e5	< 1	2.03(-0.13,+0.20)	2.9e-13(-0.4,+0.2)	10/13
500-3e5	< 0.5	1.81(-0.06,+0.07)	1.81e-12(-0.07,+0.08)	65/89